JOURNAL OF SYNCHROTRON RADIATION
ISSN 1600-5775

Exploring experimental parameter choice for rapid speckle-tracking phase-contrast X-ray imaging with a paper analyzer

Isobel A. Aloisio,[a]* David M. Paganin,[b] Christopher A. Wright[a] and Kaye S. Morgan[b]

[a]Central Medical School, Faculty of Medicine, Nursing and Health Sciences, Monash University, Clayton, VIC 3800, Australia, and [b]School of Physics and Astronomy, Monash University, Clayton, VIC 3800, Australia. *Correspondence e-mail: isobelaloisio@gmail.com

Received 9 March 2015
Accepted 12 June 2015

Edited by A. Momose, Tohoku University, Japan

Keywords: X-ray imaging; phase contrast; phase retrieval; speckle imaging.

Phase-contrast X-ray imaging using a paper analyzer enables the visualization of X-ray transparent biological structures using the refractive properties of the sample. The technique measures the sample-induced distortions of a spatially random reference pattern to retrieve quantitative sample information. This phase-contrast method is promising for biomedical application due to both a simple experimental set-up and a capability for real-time imaging. The authors explore the experimental configuration required to achieve robustness and accuracy in terms of (i) the paper analyzer feature size, (ii) the sample-to-detector distance, and (iii) the exposure time. Results using a synchrotron source confirm that the technique achieves accurate phase retrieval with a range of paper analyzers and at exposures as short as 0.5 ms. These exposure times are sufficiently short relative to characteristic physiological timescales to enable real-time dynamic imaging of living samples. A theoretical guide to the choice of sample-to-detector distance is also derived. While the measurements are specific to the set-up, these guidelines, the example speckle images, the strategies for analysis in the presence of noise and the experimental considerations and discussion will be of value to those who wish to use the speckle-tracking paper analyzer technique.

1. Introduction

Phase-contrast X-ray imaging (PCXI) allows soft tissue discrimination of X-ray-transparent biological samples, with contrast improvements and the additional possibility of smaller radiation doses when compared with conventional absorption-based imaging (Paganin *et al.*, 2002; Zambelli *et al.*, 2010). As such, PCXI is increasingly used in biomedical research and shows potential for future clinical application (Castelli *et al.*, 2011; Olivo & Castelli, 2014). However, many existing phase-contrast methods require multiple exposures for quantitative phase retrieval and thus do not permit the quantitative imaging of dynamic samples. Propagation-based phase-contrast imaging is a simple single-exposure method suitable for live imaging, and provides useful edge enhancement but has limited sensitivity to slowly varying phase gradients (Gureyev *et al.*, 2009). More sensitive techniques include crystal analyzer-based (Davis *et al.*, 1995; Ingal & Beliaevskaya, 1999) and interferometric methods (Momose *et al.*, 2003; Pfeiffer *et al.*, 2006). However, multiple images are usually required for phase retrieval using these techniques. Some quantitative information can be gained from a single image, but this requires assumptions, for example regarding sample composition (Paganin *et al.*, 2002).

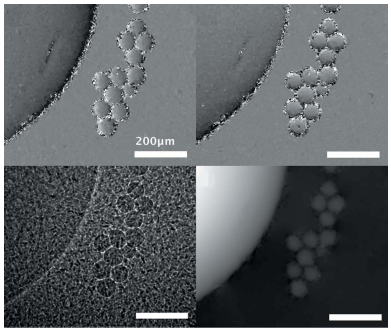

Morgan *et al.* (2012) and Berujon *et al.* (2012) first described a single-image 'paper analyzer' or speckle-tracking method that is sensitive to slowly varying phase gradients and can extract differential phase information in two directions from a single exposure, combining them to give quantitative phase depth. The technique uses the sample-induced distortion of a spatially random reference pattern to extract this differential phase contrast. A spatially random phase mask is responsible for creating the detailed high-contrast reference pattern *via* propagation-based phase contrast, making the technique inexpensive and practical. The paper analyzer technique has the set-up simplicity and speed of propagation-based PCXI, as well as the imaging sensitivity to small transverse phase shifts seen with crystal analyzer and interferometric methods. As such, this method is effective for the imaging of dynamic processes using short single-exposure times.

Whilst the paper analyzer technique has been demonstrated with both sandpaper and biological filtering membrane as the reference pattern (Berujon *et al.*, 2012; Morgan *et al.*, 2012), it is unknown how sensitive the experimental set-up is to the phase reference objects. Similarly, the choice of imaging parameters required to achieve accurate phase retrieval is not well defined. In this paper, we first study the effect of the feature size of the phase mask on the achievable sample size resolution and the accuracy of the image reconstruction. Secondly, we look at the analysis of noisy images to push the limits of exposure time to enable high-speed imaging of dynamic processes. Finally, we consider the effect of sample-to-detector distance on the reconstructed image quality. As propagation distance increases we increase phase contrast and the magnitude of the sample-induced transverse shift in the reference pattern, at the expense of a loss in flux and increasing artifacts from propagation-based fringes at the edges of the sample. We formulate some general rules that can be used to guide propagation distance selection.

2. PCXI using a paper analyzer

The simple experimental set-up is shown in Fig. 1. First, an incident X-ray wave is distorted by the paper analyzer and using propagation-based X-ray imaging produces a 'reference' speckle pattern around 1 m downstream of the sandpaper. The sample is then introduced a few centimeters downstream of the paper analyzer, which, with further propagation, produces a slightly distorted 'sample-and-reference' speckle pattern as a result of the phase changes induced by the differing refractive indices and thickness of the sample. Local transverse shifts in the spatially random speckles of the reference image occur when the sample changes the local direction of propagation of the X-ray wavefront, hence distorting the pattern observed downstream at the detector.

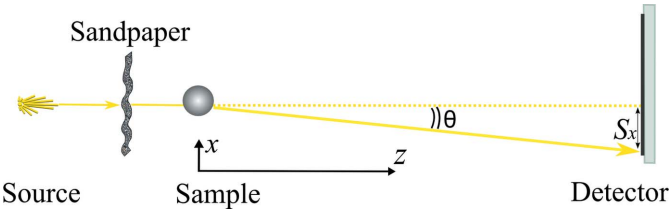

Figure 1
Experimental set-up for quantitative single-exposure phase-contrast imaging using a random phase mask. Here X-rays from a source pass through a piece of sandpaper to produce a 'reference' speckle pattern. The yellow dotted line represents an X-ray reaching the detector in the absence of any sample. A sphere is introduced downstream of the sandpaper and results in a change in the direction of propagation of the X-ray wavefront, shifting the pattern downstream, as represented by the yellow arrow. The transverse shift is represented here by S_x. The shift is also resolved into the y component S_y.

The transverse local shifts of the speckles in the reference pattern are then determined at each position (x, y) using a cross-correlation technique. An interrogation window is placed around each pixel in the 'sample-and-reference' image and is scanned to locate the same reference pattern at the original position in the reference image. A variety of feature tracking techniques have been developed, each with benefits and limitations, as described by Lewis (1995). However, few comparisons have been made between these. Normalized cross-correlation is preferred in order to overcome the variations in image intensity that occur across the interrogation field, and cross-correlation is performed in the Fourier domain for computational speed. Other techniques may pose difficulties for use with highly speckled reference images, as some require adequate low-frequency information or result in errors in the presence of textured images (Lewis, 1995). The cross-correlation analysis used in the experiments is described in detail by Morgan *et al.* (2011*a*). The transverse shift, $\mathbf{S}(x, y) = [S_x(x, y), S_y(x, y)]$, required to locally align the images, is resolved into x and y components S_x and S_y to give two differential phase-contrast images. A typical experimental result is shown in Fig. 2, where panel (*a*) shows the horizontal components S_x of the shift, and panel (*b*) shows the vertical components S_y of the shift at each location across the image. Experimental details are discussed in §3.

Two sample phase gradients $\partial\varphi/\partial x$ and $\partial\varphi/\partial y$ are calculated from the two shift images (S_x and S_y) and integrated according to the Fourier derivative theorem (Kottler *et al.*, 2007; de Jonge *et al.*, 2008) to give

$$\varphi(x, y) = k\,\mathcal{F}^{-1}\left(\mathcal{F}\left\{\tan^{-1}\left[\frac{S_x(x, y)}{z}\right] + i\tan^{-1}\left[\frac{S_y(x, y)}{z}\right]\right\} \Big/ \left(ik_x - k_y\right)\right), \quad (1)$$

where $\varphi(x, y)$ is the sample phase depth, for radiation with a wavenumber k, and sample-to-detector distance z, where $\mathcal{F}$ denotes the Fourier transform with respect to (x, y) and k_x and k_y are the Fourier-space coordinates corresponding to (x, y).

The resulting phase depth map of the spheres is shown in Fig. 2, where panel (*d*) shows the two-dimensional grayscale map, and panel (*e*) shows the three-dimensional projected phase depth. The projected thickness can be calculated from the phase depth for a homogeneous sample of thickness $T(x, y)$ and complex refractive index decrement δ [where $\varphi(x, y) = -k\delta T(x, y)$].

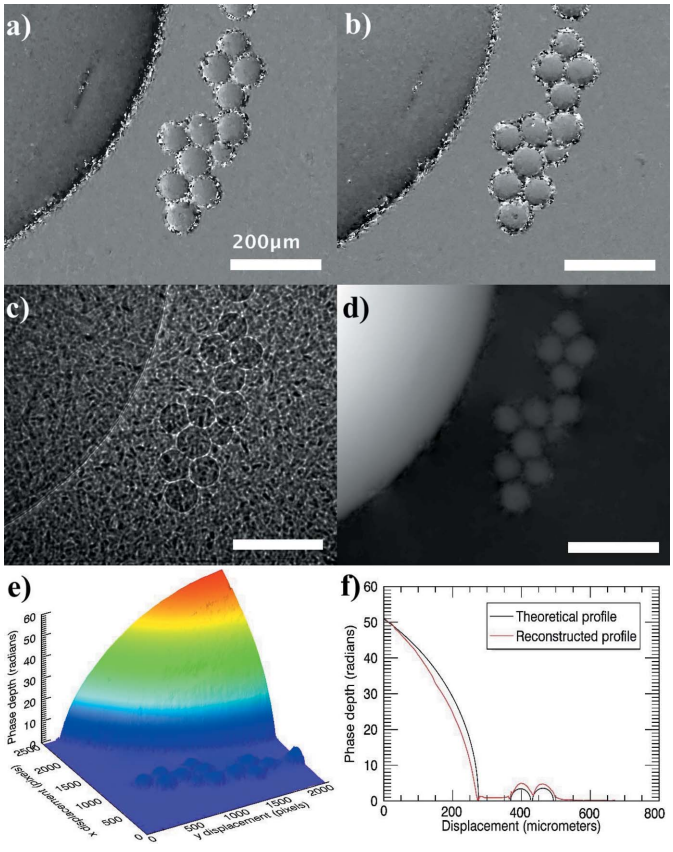

Figure 2
Differential shift images: (*a*) $S_x(x, y)$ and (*b*) $S_y(x, y)$. Here the sample comprises both glass and Perspex spheres ranging from 63 μm to 1.5 mm in diameter. The smallest feature size sandpaper is used in this figure, with a grain size of 15.3 μm, and the sample-to-detector distance is set at 75 cm. These differential shift images are calculated from the transverse shifts in speckle pattern that occur in the 'reference and sample' image (*c*). The two differential shift images are then used to reconstruct a projected phase depth of the sample (*d*) which can also be shown as a three-dimensional surface plot (*e*). A comparison is made between the reconstructed quantitative phase depth and the theoretical phase depth by taking a profile of the reconstructed image (*f*).

Profiles of the retrieved sphere thickness taken using the paper analyzer method were compared with a theoretical projected thickness, using the normalized root-mean-square (RMS) error as a measure of accuracy, defined as

$$\text{RMS error} = \left(\frac{\sum_m \left| T_{\text{T}}^m - T_{\text{R}}^m \right|^2}{\sum_m \left| T_{\text{T}}^m \right|^2} \right)^{1/2}. \qquad (2)$$

Here, T_{T} is the theoretical sample thickness, T_{R} is the reconstructed sample thickness, and m is the integer pixel co-ordinate. A comparison between the profiles of a reconstructed image and the theoretical image is shown in Fig. 2(*f*). The RMS error was calculated for the entire profile, to encompass both spheres and the vacuum space in between.

3. Experiment

We assessed the effect of changing imaging parameters, including (i) the paper analyzer feature size, (ii) propagation distance and (iii) exposure time. To do this we compared images of both Perspex spheres of diameter 1.5 mm and glass spheres with a specified diameter size range of 63–75 μm in order to test the paper analyzer technique on materials of different refractive indices, sizes and phase gradients (a perfect sphere, according to the projection approximation, provides phase gradients from zero to infinity in all directions). A simple phantom is also required in order to calculate an accurate theoretical thickness to compare with the experimental retrieved thickness.

Images were acquired at the biomedical imaging beamline BL20XU at the SPring-8 synchrotron facility, Hyogo, Japan. A crystal Si-111 monochromator was used to select X-rays at an energy of 25 keV. The source-to-sample distance was 245 m and the sample-to-detector distance was varied between 25 cm and 100 cm. The paper random phase mask was placed 7 cm before the sample. The detector system comprised a 2560 × 2160 pixel sCMOS camera (pco.Edge) and a YAG 30 μm-thick phosphor with a 20× magnification lens to give an effective pixel size of 0.29 μm.

The sample comprised Goodfellows ME306810/3 PMMA (Perspex) 1.5 mm spheres with a ±5% tolerance in diameter, and glass spheres with a specified diameter size range of 63–75 μm. The sample was imaged using eight types of KMCA silicon carbide electro-coated abrasive sandpaper with different grain sizes as the paper analyzer. Two pieces of paper were also used: a piece of paper towel and a piece of Reflex Ultra White A4 Paper. Images were also recorded at exposure times of 0.5 ms, 1 ms, 5 ms and 10 ms. In all cases the speckle features were resolved by the detector, which is a limiting factor since reconstruction is impossible if this criterion is not met. We focused on increasing the analyzer feature size with respect to the sample feature size.

When performing the cross-correlation computation, an interrogation window (20 × 20 pixels) was stepped pixel by pixel for a total shift of 10 pixels in both the horizontal and vertical planes, in order to locate the sample-induced distortions of the reference image. This interrogation window was sufficiently large to always include a reference feature, but not so large as to smooth out sample features. Ten pixels was the maximum shift observed in the images. Image profiles were aligned manually to perform RMS error evaluation. The variation in RMS error was less than 0.2% for shifts of ten pixels relative to the aligned position for the different paper analyzers, and less than 1% for different exposure times and propagation distances. This can be taken as an indication of the magnitude of error bars on the plots below.

4. Results

4.1. Paper analyzer

A plot of the RMS error in the reconstructed sample projected thickness for each of the different types of sandpaper and two types of paper is shown in Fig. 3. The profiles for each of the eight pieces of sandpaper showed good correspondence with a normalized RMS error of less than 9%

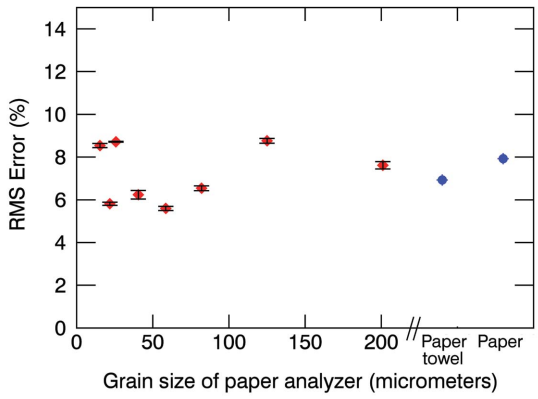

Figure 3
RMS error in recovered phase depth for eight pieces of sandpaper with different grain sizes ranging from 15.3 μm to 201 μm (red dots), together with a piece of paper towel or a piece of Reflex Ultra White A4 Paper as the analyzer (blue dots). The sample-to-detector distance was set at 75 cm. As mentioned in §4.1, the variation in RMS error was less than 0.2% for shifts of ten pixels relative to the aligned position. The error bars are less than 0.2% RMS error, which is smaller than the data points.

for all papers tested. The lowest error was 5.6%, achieved with the sandpaper of 58.5 μm feature size. This error is comparable with previous studies by Morgan *et al.* (2011*a*), which obtained a normalized RMS error of 3.2% on the same 1.5 mm Perspex spheres using a periodic grating in place of the sandpaper. The vacuum error for the reconstruction was also minimal, as seen in the profile of Fig. 2(*f*). Using sandpaper of grain size 15.3 μm, the retrieved phase depth of the vacuum had a mean error of 1.6 rad in the presence of 50 rad features.

Fig. 3 demonstrates that in our images the RMS error does not change significantly with increasing grain size. This is despite the average grain size ranging from 15 μm to 200 μm. Images of four different pieces of sandpaper are shown in Figs. 4(*a*)–(*d*).

The sandpaper image shows that all the pieces of sandpaper had a similar high-frequency reference pattern in the background despite their differing average grain size. This is likely due to the texture of the paper, which supports the sand grains, as well as the glue that binds the grains onto the paper. To confirm this observation we performed a rotationally averaged autocorrelation on each of the sandpaper images, which is shown in Fig. 5.

In spite of the great variation in grain sizes and contrast across the sandpaper, the paper analyzer technique was able to utilize the high-frequency background features as a reference pattern and reconstruct images with an approximately uniform RMS error calculated for each of the different pieces of sandpaper. This result is testament to the robustness of the technique to a range of reference objects. Even the coarsest sandpaper (Fig. 4*d*) with very strong propagation-based fringes seen at the grain edges and varying contrast across the reference image (inside/outside/at the edges of grains) achieved a reconstruction with only 7.6% error. This is in contrast to grating interferometry and spatial harmonic methods where grating imperfections can lead to artifacts or loss of contrast (Bech *et al.*, 2009; Olivo *et al.*, 2009; Wen *et al.*,

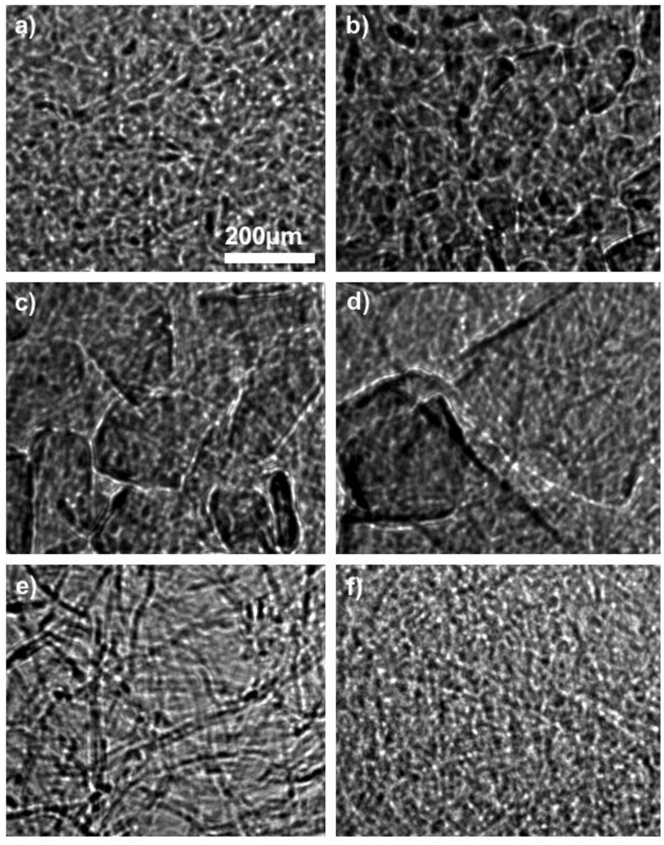

Figure 4
Cropped and magnified PCXI reference images of six different materials used as a paper analyzer: (*a*) sandpaper of 15.3 μm feature size, (*b*) sandpaper of 40.5 μm feature size, (*c*) sandpaper of 82 μm feature size, (*d*) sandpaper of 201 μm feature size, (*e*) paper towel used as an analyzer, (*f*) Reflex Ultra White A4 Paper used as an analyzer. The sample-to-detector distance was set at 75 cm. The visibility (calculated using Michelson's definition, after eliminating outliers, that is those pixels occupying a gray level outside the central histogram peak, with the central peak edges defined as where the number of pixels of that gray level falls below 5 in the 2560 × 2160 image) for panels (*a*)–(*f*) are 0.93, 0.97, 0.95, 0.96, 0.88 and 0.82, respectively. Measuring visibility using a profile across the image (as performed with regular grid patterns) gives a visibility of 0.55–0.60 for the sandpapers and 0.35–0.40 for the tissue papers. A linear grayscale from 400 to 19000 is used for images (*a*)–(*d*), and from 4000 to 11000 for images (*e*) and (*f*).

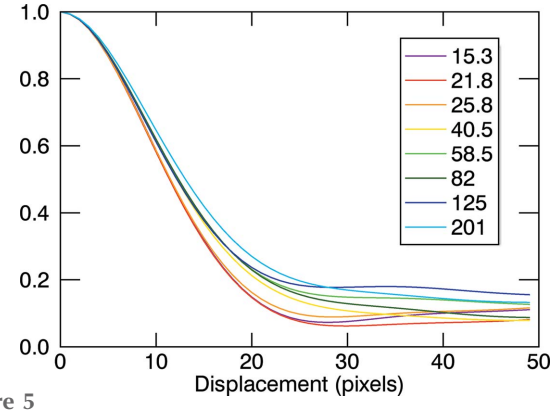

Figure 5
The rotationally averaged autocorrelation functions of the different pieces of sandpaper are represented by different colored lines. The legend lists the sandpaper grain size in micrometers corresponding to the matching line color. The autocorrelation function is at a peak when there is no displacement and the peak height is normalized to 1.

2010). Image reconstruction was performed using both a piece of paper towel and a piece of printer paper as the analyzer, with an RMS error of 6.9% and 7.9%, respectively, which shows how simple and inexpensive the optics for this method can be, particularly when using a highly coherent X-ray source. Random phase objects will also avoid aliasing artefacts when imaging periodic objects, in contrast to purpose-built periodic grids. Moreover, there is a possibility that the image imperfections caused by rough or imperfect optical elements could in fact be utilized in or as the speckled reference pattern, turning what is ordinarily detrimental to an imaging system into a constructive component of the imaging process. It is recognized that a purpose-built analyzer has the advantage of being able to analyze with maximum sensitivity in a particular direction and can create reference patterns of optimized visibility for reliable tracking of reference pattern shifts in the presence of noise.

More detailed characterization of the speckle reference patterns could calculate the characteristic length scale distribution, in order to select an analyzer to provide the required reconstructed image resolution. The angular accuracy is limited by the detector pixel size and the sample-to-detector distance (Morgan *et al.*, 2013; Berujon *et al.*, 2012), but can also be degraded in the presence of noise and a low-visibility reference pattern with slowly varying features. In general, the main requirement for high-quality imaging is that the reference pattern is consistent across the image and that features are high contrast, well-resolved and, in size, of the order of resolution that is desired. If the reference pattern features are too close to the detector pixel size, such that they cannot be well resolved, this will result in poor reference pattern visibility, and the features will be difficult to track in the presence of noise.

4.2. Exposure time

We compared the reconstructed profiles from raw images taken with four different exposure times of 0.5 ms, 1 ms, 5 ms and 10 ms, using the smallest sized grain sandpaper (15.3 µm) as the paper analyzer. Before image reconstruction, four different pre-processing methods were applied to the raw images in order to determine a suitable method for reducing noise levels and thus improving the quality of the reconstructed images at ultra-short exposure times. A plot of the RMS errors in the phase retrieval as a function of exposure time, on a single raw image and after each of the four pre-processing methods, is shown in Fig. 6, and the five methods are outlined in detail in the caption.

Using a single unfiltered image for analysis, the RMS error of the reconstructed images decreased considerably with increasing exposure time (from 46.3% at 0.5 ms to 15.2% at 10 ms). This was expected due to the decreased noise in images with longer exposures. Averaging 20 images together also decreases the detector noise due to random fluctuations. However, at an exposure of 0.5 ms, averaging 20 images resulted in the largest RMS error of 59.7%. At very short exposure times, dark current dominates the image. We estimate that the 0.5 ms exposure image is in fact only 31% X-ray signal and 69% dark current, found by plotting the number of counts against exposure time for all images. Averaging these short exposure images decreases the amount of noise present, leaving not only a stronger X-ray signal but also a stronger image of the structured component of the dark current. When this structured dark current makes up a larger proportion of the image than the X-ray signal, the speckle-tracking analysis 'tracks' the position of the dark current instead of the X-ray signal, biasing the detected 'shift' towards zero and decreasing the quality of the reconstructed image. These errors can be seen in Fig. 7, which shows the differential vertical shift S_y obtained (*a*) when using the average of 20 images at 0.5 ms exposure for analysis, and (*b*) when using the single image at 0.5 ms exposure, respectively. Note that the high-frequency noise seen in Fig. 7(*b*) is damped during the integration when reconstructing the projected sample thickness. In Fig. 7(*a*) the speckle-tracking process biases towards no shift (gray) since the dominant dark current and hot pixels do not shift and therefore the process fails to detect the vertical gradient across the spheres. The high-frequency low-count noise in the single exposure is of a similar frequency to the dark current and hot pixels and hence can help to 'drown out' the structure inherent in the detector images. We attempted to 'correct' for the dark current by subtracting an averaged dark-current image from both the reference speckle image and the sample-and-reference speckle image. While subtracting the dark current from either one of these images reduced the problem of the bias towards zero shift, if the dark current image was subtracted from both these images this actually increased the similarity of the two images (particularly given that the dark-current signal

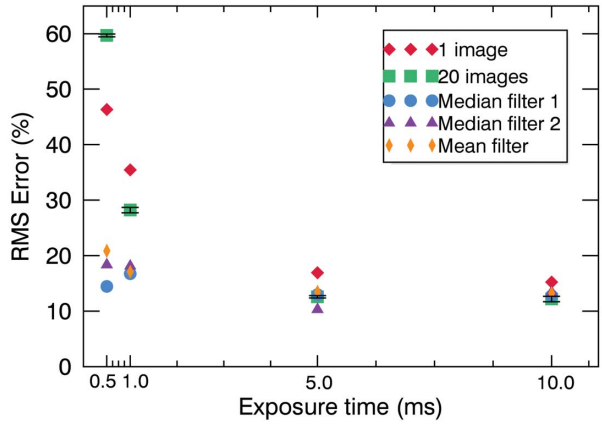

Figure 6
Comparison of RMS error values for different exposure times of 0.5 ms, 1 ms, 5 ms and 10 ms, and different pre-processing methods. 1 image: a single image taken at each exposure time was left unprocessed and the phase depth was reconstructed; 20 images: the average of 20 images taken with the same exposure time; Median filter 1: a median filter with a radius of 10 pixels was first applied to the single raw image; Median filter 2: a median filter with a radius of 5 pixels was first applied to the single raw image; Mean filter: a mean filter with a radius of 5 pixels was first applied to the single raw image. Note that the reference image was taken with a 100 ms exposure time for all reconstructions; given a high signal-to-noise ratio reference is best practice and not difficult to acquire experimentally. The error bars are less than 0.5% RMS error, which is smaller than the data points.

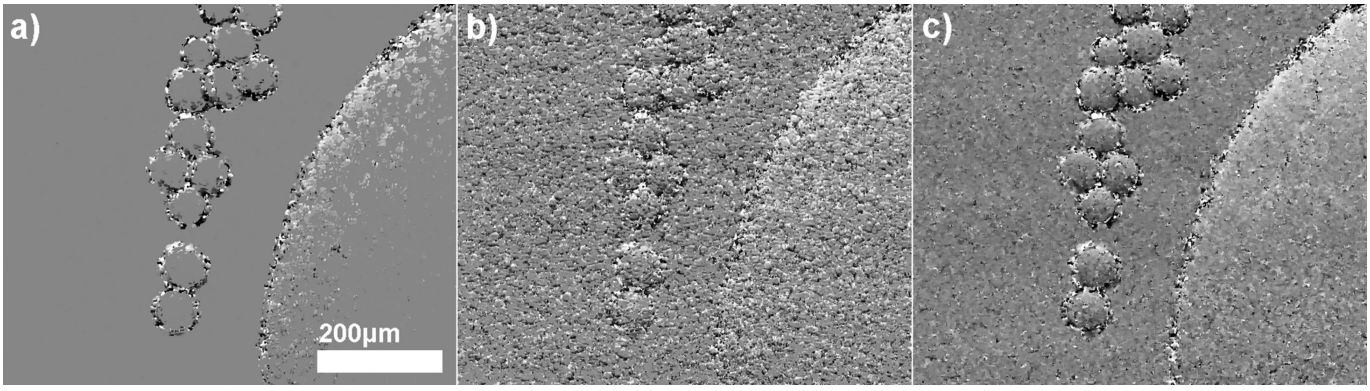

Figure 7
Differential shift images: (*a*) $S_y(x, y)$ with the average of 20 images at 0.5 ms exposure used for analysis, and (*b*) $S_y(x, y)$ with a single image at 0.5 ms exposure used for analysis. The differential shift image obtained using the average of 20 images, as shown in (*a*), fails to detect the vertical gradient across the spheres because of a stationary and structured dark current, resulting in the visibly uniform gray appearance. In spite of the high-frequency noise seen in (*b*), the differential shift image obtained using a single image shows the change in gradient across the spheres. When these images are integrated to give the total thickness, (*b*) gives a considerably more accurate reconstruction. Our best differential phase reconstruction at 0.5 ms is shown in (*c*), which was reconstructed using a single sample-and-reference image with only high-frequency noise filtering, to a 20-image-averaged reference speckle image with both dark-current subtraction and high-frequency noise filtering.

occupied more gray levels than the speckle signal), and increased the problem of a bias towards zero shift. A similar effect is seen with a flat-field correction. Filtering out high-frequency noise (by median-filtering any pixels that were greater than two standard deviations from the gray-level value of their neighbors) was more effective at removing dark current and hot pixel structure without introducing similarities between the speckle reference and the sample-and-reference speckle images. Fig. 7(*c*) shows our best differential phase reconstruction at 0.5 ms, the result of comparing a single sample-and-reference speckle image (with high-frequency noise filtering but no dark-current subtraction) to a 20-image-averaged reference speckle image, that has undergone both dark-current subtraction and high-frequency noise filtering.

The Median filter 1, Median filter 2 and Mean filter all resulted in consistently low RMS errors for each of the reconstructed images. At 0.5 ms exposure we obtained an RMS error of only 14.5% using the Median filter 1, which is comparable with the most accurate reconstruction with an RMS error of 12.2% achieved with an exposure of 10 ms (20 times longer). Overall, the Median filter 1 (10 pixel radius) produced the most accurate reconstructions. The significant decrease in RMS error associated with applying the Median filter 1 is promising in terms of achieving high-quality images with greatly reduced exposure time and radiation dose. Note that if the reference pattern contained higher-frequency signals and/or the propagation distance was shorter, the filter width may need to be decreased in order to preserve the position and visibility of the shifted reference features.

Previous experiments using the paper analyzer method (Morgan *et al.*, 2012) were able to visualize samples with an exposure time of 150 ms. We have demonstrated accurate phase retrieval with exposures as short as 0.5 ms. These exposure times are sufficiently short, relative to characteristic physiological timescales, to enable real-time imaging of dynamic samples. Real-time imaging enables us to visualize changes in physiological systems, and a future application of the paper analyzer technique is the *in vivo* imaging of function.

4.3. Propagation distance

The accuracy of the reconstructed phase depth was evaluated at propagation distances of 25 cm, 50 cm, 75 cm and 100 cm and the reconstruction of the small Perspex spheres was compared with the larger glass sphere at each of these propagation distances. To evaluate the effect of propagation on the detection of different phase gradients across the sphere the RMS error value for the thickness profile near the edge of the Perspex sphere was compared with the thickness profile in the bulk of the sphere. The very edges of the sphere (where the sphere meets air) were excluded from this RMS error calculation as they have considerably larger error values due to propagation-based fringes that affect the reconstruction process. We sought to eliminate this error in order to more fairly compare reconstructions from the large phase gradients towards the edge of the sphere with the smaller phase gradients in the bulk of the sphere. Each of these plots is shown in Fig. 8.

Overall the profile error decreased with an increase in the propagation distance, with considerable improvement in reconstruction from 29.8% error at 25 cm to 10.7% error at 100 cm. This result is expected, as the transverse shift induced by the sample will increase with propagation and therefore be more easily detected (Bennett *et al.*, 2010; Morgan *et al.*, 2012).

Whilst the reconstruction of the large spheres improved with increasing distance, the reconstruction of the small spheres did not and had poor correspondence with all RMS errors above 50%. The propagation-based phase-contrast fringes from the edges of the small spheres are comparable in size with the spheres themselves and so affect the quality of the reconstruction, seen in Figs. 2(*a*) and 2(*b*). The fringes

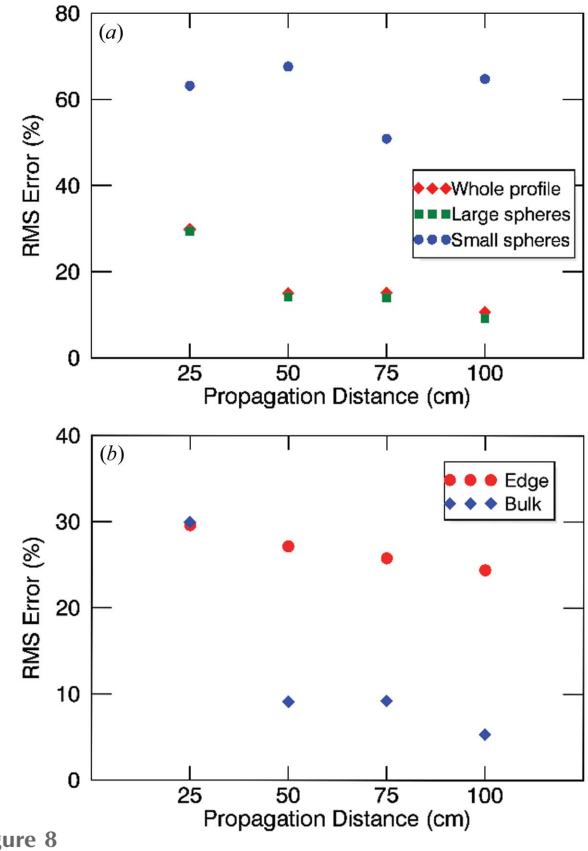

Figure 8
Comparison of the RMS error values at different sample-to-detector propagation distances. (*a*) RMS error (%) expressed at sample-to-detector distances of 25, 50, 75 and 100 cm. A comparison is made between the error of the whole profile as seen in red, the error of the large Perspex sphere as seen in green, and the error of the small glass spheres as seen in blue. (*b*) RMS error (%) expressed at the same sample-to-detector distances. A comparison is made between the reconstruction near the edge of the large Perspex sphere and the bulk of the Perspex sphere. The error bars are less than 1% RMS error, which is smaller than the data points and so are not shown.

impact significantly on the ability to track the sample-induced shifts in the reference image and subsequently lead to poor edge reconstruction, which is visualized in Fig. 2(*f*) with the comparison of the theoretical profile with the reconstructed profile. These errors represent a significant proportion of the total thickness at the edge of the sphere, and thus result in high RMS error values. Morgan *et al.* (2012) proposed the potential for more advanced phase extraction techniques, which could use the reconstructed spheres to estimate propagation-based fringes and then subtract these before performing the cross-correlation analysis, thus minimizing the impact of edge artifacts. Future work could also look at combining contrast mechanisms using the ideas presented by Pavlov and colleagues for unifying analyzer-based PCXI with propagation-based PCXI (Pavlov *et al.*, 2004, 2005). It is also possible that the spatial resolution of the technique is limiting the accuracy of these smaller sample features, an issue encountered in all imaging modalities. In previous studies using this technique, the reconstruction of a 3 mm cylinder produced an RMS error of 1.8% (Morgan *et al.*, 2011*b*), whereas the reconstruction of a 1.5 mm sphere resulted in an error of 3.2% (Morgan *et al.*, 2011*a*). The paper analyzer technique trades spatial resolution for increased speed of imaging and sensitivity to slowly varying phase gradients. Whilst the quantitative analysis of the small glass spheres in our study was not very accurate, images were still qualitatively good and closely resembled the sample. This reaffirmed that the phase reconstruction technique is best suited to slowly varying samples that do not provide significant edge enhancement.

As with our previous observations, the reconstruction of both the low-gradient and high-gradient regions of the larger sphere improved with increasing sample-to-detector propagation. There were two main findings from this comparison. Firstly, the low-gradient region of the sphere had a more accurate reconstruction than the high-gradient region of the sphere at all propagation distances excepting 25 cm. This first observation is somewhat unexpected. Although the paper analyzer technique measures the first derivative of the phase and is therefore more sensitive to slowly varying phase gradients than propagation-based methods (Morgan *et al.*, 2012), we would still expect the strong diffraction that occurs towards the edge of samples to create a transverse shift that was more easily detectable, and hence the high-gradient region would be more accurately reconstructed. A possible explanation for this is again the normalized RMS error calculation. The thickness of the sphere is greatest in the center of the sphere and so any errors in the measured gradient here make a comparatively small contribution to the total thickness. We also know that the propagation-based fringes that occur at the edges of samples can lead to poor reconstruction and this could explain the high error values calculated for the edges of the 1.5 mm sphere. The less accurate reconstruction at 25 cm could result from the weak phase gradients towards the center of the sphere, which would cause only a small transverse shift at such a short propagation distance. Because the image we evaluate is reconstructed using integration, each pixel in the reconstructed image uses information from surrounding pixels in the gradient image. Hence, the errors in the low-gradient regions of the thickness image come from errors in both the high- and low-gradient regions of the gradient image.

Secondly, the accuracy of the reconstructed projected thickness of the bulk of the sphere improved more dramatically with increased sample-to-detector distance, which was to be expected. The paper analyzer technique is more sensitive to weak phase gradients at longer sample-to-detector distances because the magnitude of the transverse reference pattern shift will increase with propagation and thus be more easily detected (Morgan *et al.*, 2012). Comparatively, the high-gradient region of the spheres will refract the X-rays more strongly and thus create a transverse shift that is more easily detected at shorter propagation distances (Morgan *et al.*, 2012).

Selection of a suitable propagation distance is important when considering biomedical applications, which may require visualization of particular features of a specimen. We desire a sample-to-detector distance long enough to create phase contrast so that we can detect the sample-induced transverse

shift, whilst also maintaining a high flux so that we can image moving structures with short exposure times, and decrease the radiation dose (Wu & Liu, 2003). An increased propagation distance also leads to increased edge artifacts, disrupting the phase retrieval. Our experiment was limited because we only imaged up to a propagation distance of 100 cm and did not reach a maximum distance at which the accuracy of the technique decreased, as was seen in Morgan *et al.* (2013) with a phase grid. We, therefore, consider theoretically the factors that affect the optimal propagation distance. These considerations also mean the results are more generally applicable.

5. Theoretical propagation distance calculations

Our first consideration is the optimal distance for detecting transverse shift $\mathbf{S}(x, y)$. As propagation distance increases, the transverse shift $\mathbf{S}(x, y)$ will increase. The maximum propagation distance, z, beyond which the transverse shift can no longer be definitely tracked, will occur when the shift $\mathbf{S}(x, y)$ is equal to the speckle feature size, L. We will consider this problem in one dimension, x. We know that $\tan\theta = S_x/z$. Rearranging this, and using the small-angle approximation ($\tan\theta \simeq \theta$ for small θ) we arrive at

$$z_{\text{maximum shift}} \simeq L/\theta. \tag{3}$$

Fig. 9 shows a sample feature of size T, approximated as a sphere of diameter T, from which the average phase gradient can be calculated as

$$\left|\frac{\partial\varphi}{\partial x}\right| \simeq \frac{Tk\delta}{T/2} = 2k\delta. \tag{4}$$

It holds that for radiation with a wavenumber k, and a sample with phase depth $\varphi(x, y)$, the sample will diffract the incident beam by angle θ_x according to

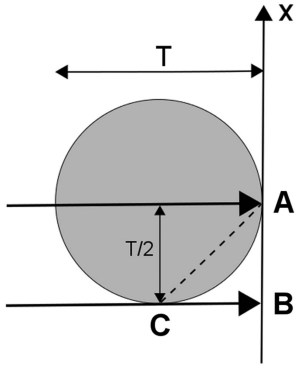

Figure 9
Calculating the average phase gradient of a sphere. Arrow A depicts an X-ray passing through a sample sphere of thickness T. Arrow B depicts an X-ray passing through a vacuum on the edge of the sphere. The phase gradient of the curve connecting points A and C is approximated by the gradient of the dotted line. The distance between A and B along the x-axis can be described as the change in distance between A and B, which is equal to $T/2$. This distance is equal to distance BC. The change in phase between points A and B is described as $\Delta\varphi$. The phase change incurred by the sample by point $A = -k\delta T$ where δ is the refractive index decrement corresponding to the refractive index $n = 1 - \delta$. The phase change incurred by the sample by point $B = 0$. The phase difference, $\Delta\varphi$, between A and B is $-Tk\delta$.

$$|\theta_x| = \frac{1}{k}\left|\frac{\partial\theta}{\partial x}\right|. \tag{5}$$

Substituting (5) into (4) we arrive at

$$2\delta \simeq |\theta|. \tag{6}$$

We then substitute this into (3) to give our final result,

$$z_{\text{maximum shift}} \simeq \frac{L}{\theta} \equiv \frac{L}{2\delta}. \tag{7}$$

Equation (7) shows that the maximum propagation distance is directly proportional to the speckle feature size and inversely proportional to the refractive index decrement, δ, of the sample. For our experimental conditions, an analyzer producing a reference pattern with feature size 15 µm and sample δ value of 3.5×10^{-7}, we can increase the propagation distance to 21.4 m. However, this propagation distance is unrealistic as there would be a significant drop in flux (particularly without a vacuum tube) as well as poor reconstruction due to propagation-based fringes at the edges of the sample (Gureyev *et al.*, 2009). We also note that this maximum distance is calculated for the 'average' gradient of the sample feature [as seen in equation (4)]. If we were to instead reconstruct a different component of the sample sphere (for example, imaging the steeper-than-average part of the large sphere) where the gradient is steeper, the maximum distance would be shorter. Using this method, one can calculate the propagation distance at which any part of the sample will be unable to be accurately reconstructed. For example, at 10% of the thickness from the edge of the sample the phase change is given by

$$\Delta\varphi = k\delta\left[(T/2)^2 - (0.9T/2)^2\right]^{1/2} = 0.218k\delta T. \tag{8}$$

The phase gradient can then be calculated using

$$\frac{\partial\varphi}{\partial x} = \frac{0.218k\delta T}{(T/10)} = 2.18k\delta. \tag{9}$$

Using (7), the maximum propagation distance can be calculated,

$$z_{\text{maximum shift}} \simeq L/2.18\delta. \tag{10}$$

This is equal to 19.7 m in our case. It is important to note that equation (7) also demonstrates that the maximum propagation distance is not dependent upon the sample feature size, T, or directly dependent on the wavelength of the radiation, λ, simplifying the propagation distance problem.

Our second consideration is the effect on image reconstruction of propagation-based fringes created by sharp sample edges. If the fringe size becomes too large compared with the feature size of the speckle, the reconstruction of the sample edges will be poor. The fringe width corresponds to the width of the first Fresnel zone F, given by (Gureyev *et al.*, 2009)

$$F = (R'\lambda)^{1/2} \quad \text{where} \quad R' = \frac{R_1R_2}{R_1 + R_2}. \tag{11}$$

Here, R_1 is the source-to-sample distance and R_2 is the sample-to-detector distance.

Rearranging (11) to give sample-to-detector distance R_2 in terms of R_1, fringe width F and wavelength λ,

$$R_2 = \frac{R_1 F^2}{\lambda R_1 - F^2}. \quad (12)$$

We then let fringe width F equal a fraction of the speckle feature size L, so that $F = L/a$. The result is the maximum distance as defined by the sample edge fringes, given by

$$z_{\text{maximum fringe}} = \frac{R_1 (L/a)^2}{\lambda R_1 - (L/a)^2}. \quad (13)$$

Taking into consideration our experimental parameters of a source-to-sample distance of 245 m, a wavelength of 0.5×10^{-10} m and $\delta = 3.5 \times 10^{-7}$, we plot both the shift-associated maximum distance in equation (7) and the fringe width-associated maximum distance in equation (13) as a function of the speckle feature size L. The result is shown in Fig. 10. The limiting fringe width-associated sample-to-detector distance is plotted for fringe width equal to one fifth of, one tenth of, one twentieth of and equal to the speckle feature size. It can be seen that the limit to the sample-to-detector distance is far more sensitive to the increasing width of the propagation-based fringes than the transverse feature shift induced by the sample. In fact, at increasing propagation distances, the fringe width will equal the speckle feature size well before the shift-associated maximum distance is reached.

There are additional factors that affect the ideal propagation distance and achievable spatial resolution that we did not consider in our experimental or theoretical studies. These include the detector pixel size (Gureyev *et al.*, 2009; Wen *et al.*, 2010), the given flux at different propagation distances (Wu & Liu, 2007), and the point spread function of the imaging system (Gureyev *et al.*, 2009). The first two factors did not affect our experiments, as our effective pixel size of 0.29 µm was well below the speckle feature size and also small enough to detect weak phase gradients, and the bright synchrotron source had sufficient flux at all propagation distances used. However, these factors are important when considering the implementation of the technique in a clinical setting, especially if the sample is weakly diffracting or we are using a low-brilliance conventional X-ray source, as recently demonstrated by Zanette *et al.* (2014).

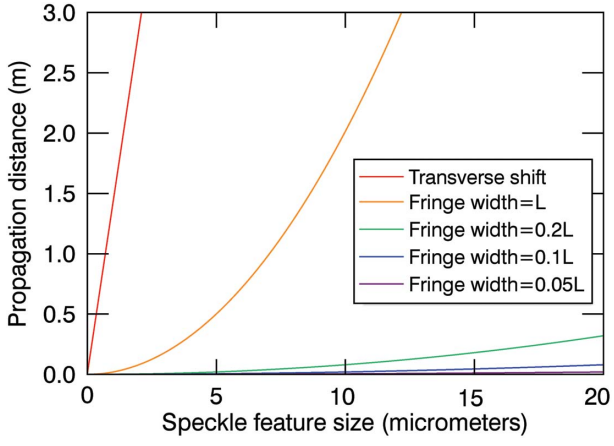

Figure 10
We compare the maximum propagation distances as defined by both the sample shift and by the sample edge fringes. The shift-associated maximum distance z for a given δ of 3.5×10^{-7} is plotted against feature size. This is represented by the red line. The purple, blue, green and orange lines represent the fringe width-associated maximum distance for a fringe width equal to a fraction of the speckle feature size (as defined in the legend). The source-to-sample distance is 245 m, λ is 0.5×10^{-10} m.

6. Conclusions

Phase-contrast X-ray imaging using a random phase mask or paper analyzer has been successfully applied to the quantitative phase retrieval of X-ray transparent samples. In particular, the technique shows promise for the imaging of dynamic samples due to its ability to accurately reconstruct images with short single-exposure times and a simple experimental set-up. However, whilst we have demonstrated the robustness of the paper analyzer method to noisy images, the next challenge is to realise dynamic imaging with these short exposure times using a conventional X-ray source, which has significantly reduced flux when compared with synchrotron X-rays. With the aid of pre-processing filters our experiments reduced exposure times by three orders of magnitude from previous work, suggesting that even with reduced flux the paper analyzer technique may still achieve accurate reconstruction with quite short exposure times. We were able to achieve accurate phase retrieval with an exposure of only 0.5 ms. Moreover, with the development of compact table-top synchrotron sources (Hirai *et al.*, 2006; Bech *et al.*, 2009), laser wakefield accelerators (Schlenvoigt *et al.*, 2008; Fourmaux *et al.*, 2011) and liquid-metal-jet sources (Hemberg, 2004; Tuohimaa *et al.*, 2007), achieving short exposure times in a clinical setting is plausible.

Acknowledgements

We thank JASRI for the use of the SPring-8 synchrotron in Japan, beamline BL20XU, under experiment 2013A1352. We acknowledge travel funding provided by the International Synchrotron Access Program (ISAP) managed by the Australian Synchrotron and funded by the Australian Government (AS_IA132). KM is supported by a DECRA from the Australian Research Council.

References

Bech, M., Bunk, O., David, C., Ruth, R., Rifkin, J., Loewen, R., Feidenhans'l, R. & Pfeiffer, F. (2009). *J. Synchrotron Rad.* **16**, 43–47.

Bennett, E. E., Kopace, R., Stein, A. F. & Wen, H. (2010). *Med. Phys.* **37**, 6047–6054.

Berujon, S., Wang, H. & Sawhney, K. (2012). *Phys. Rev. A*, **86**, 063813.

Castelli, E., Tonutti, M., Arfelli, F., Longo, R., Quaia, E., Rigon, L., Sanabor, D., Zanconati, F., Dreossi, D., Abrami, A., Quai, E., Bregant, P., Casarin, K., Chenda, V., Menk, R. H., Rokvic, T., Vascotto, A., Tromba, G. & Cova, M. A. (2011). *Radiology*, **259**, 684–694.

Davis, T. J., Gao, D., Gureyev, T. E., Stevenson, A. W. & Wilkins, S. W. (1995). *Nature (London)*, **373**, 595–598.
Fourmaux, S., Corde, S., Phuoc, K. T., Lassonde, P., Lebrun, G., Payeur, S., Martin, F., Sebban, S., Malka, V., Rousse, A. & Kieffer, J. C. (2011). *Opt. Lett.* **36**, 2426.
Gureyev, T. E., Mayo, S. C., Myers, D. E., Nesterets, Y., Paganin, D. M., Pogany, A., Stevenson, A. W. & Wilkins, S. W. (2009). *J. Appl. Phys.* **105**, 102005.
Hemberg, O. (2004). *Opt. Eng.* **43**, 1682–1688.
Hirai, T., Yamada, H., Sasaki, M., Hasegawa, D., Morita, M., Oda, Y., Takaku, J., Hanashima, T., Nitta, N., Takahashi, M. & Murata, K. (2006). *J. Synchrotron Rad.* **13**, 397–402.
Ingal, V. N. & Beliaevskaya, E. A. (1999). *J. Phys. D*, **28**, 2314–2317.
Jonge, M. D. de, Hornberger, B., Holzner, C., Legnini, D., Paterson, D., McNulty, I., Jacobsen, C. & Vogt, S. (2008). *Phys. Rev. Lett.* **100**, 163902.
Kottler, C., David, C., Pfeiffer, F. & Bunk, O. (2007). *Opt. Express*, **15**, 1175.
Lewis, J. P. (1995). *Vis. Interface*, **95**, 120–123.
Momose, A., Kawamoto, S., Koyama, I., Hamaishi, Y., Takai, K. & Suzuki, Y. (2003). *Jpn. J. Appl. Phys.* **42**, L866–L868.
Morgan, K. S., Modregger, P., Irvine, S. C., Rutishauser, S., Guzenko, V. A., Stampanoni, M. & David, C. (2013). *Opt. Lett.* **38**, 4605–4608.
Morgan, K. S., Paganin, D. M. & Siu, K. (2011*b*). *Opt. Lett.* **36**, 55–57.
Morgan, K. S., Paganin, D. M. & Siu, K. K. W. (2011*a*). *Opt. Express*, **19**, 19781–19789.
Morgan, K. S., Paganin, D. M. & Siu, K. K. W. (2012). *Appl. Phys. Lett.* **100**, 124102.
Olivo, A., Bohndiek, S. E., Griffiths, J. A., Konstantinidis, A. & Speller, R. D. (2009). *Appl. Phys. Lett.* **94**, 044108.
Olivo, A. & Castelli, E. (2014). *Riv. Nuov. Cim.* **37**, 467–508.
Paganin, D., Mayo, S. C., Gureyev, T. E., Miller, P. R. & Wilkins, S. W. (2002). *J. Microsc.* **206**, 33–40.
Pavlov, K. M., Gureyev, T. E., Paganin, D., Nesterets, Ya. I., Kitchen, M. J., Siu, K. K. W., Gillam, J. E., Uesugi, K., Yagi, N., Morgan, M. J. & Lewis, R. A. (2005). *Nucl. Instrum. Methods Phys. Res. A*, **548**, 163–168.
Pavlov, K. M., Gureyev, T. E., Paganin, D., Nesterets, Ya. I., Morgan, M. J. & Lewis, R. A. (2004). *J. Phys. D*, **37**, 2746–2750.
Pfeiffer, F., Weitkamp, T., Bunk, O. & David, C. (2006). *Nat. Phys.* **2**, 258–261.
Schlenvoigt, H. P., Haupt, K., Debus, A., Budde, F., Jackel, O., Pfotenhauer, S., Schwoerer, H., Rohwer, E., Gallacher, J. G., Brunetti, E., Shanks, R. P., Wiggins, S. M. & Jaroszynski, D. A. (2008). *Nat. Phys.* **4**, 130–133.
Tuohimaa, T., Otendal, M. & Hertz, H. M. (2007). *Appl. Phys. Lett.* **91**, 074104.
Wen, H. H., Bennett, E. E., Kopace, R., Stein, A. F. & Pai, V. (2010). *Opt. Lett.* **35**, 1932–1934.
Wu, X. & Liu, H. (2003). *Med. Phys.* **30**, 2169–2179.
Wu, X. & Liu, H. (2007). *Med. Phys.* **34**, 737–743.
Zambelli, J., Bevins, N., Qi, Z. & Chen, G.-H. (2010). *Med. Phys.* **37**, 2473–2479.
Zanette, I., Zhou, T., Burvall, A., Lundström, U., Larsson, D. H., Zdora, M., Thibault, P., Pfeiffer, F. & Hertz, H. M. (2014). *Phys. Rev. Lett.* **112**, 253903.